

See discussions, stats, and author profiles for this publication at: <https://www.researchgate.net/publication/8053460>

Numerical Simulation of Scanning Electrochemical Microscopy Experiments with Frame-Shaped Integrated Atomic Force Microscopy–SECM Probes Using the Boundary Element Method

ARTICLE *in* ANALYTICAL CHEMISTRY · MARCH 2005

Impact Factor: 5.64 · DOI: 10.1021/ac048732n · Source: PubMed

CITATIONS

33

READS

27

7 AUTHORS, INCLUDING:



Christine Kranz

Universität Ulm

130 PUBLICATIONS **2,449** CITATIONS

SEE PROFILE



Boris Mizaikoff

Universität Ulm

311 PUBLICATIONS **4,800** CITATIONS

SEE PROFILE



Alois Lugstein

TU Wien

129 PUBLICATIONS **1,726** CITATIONS

SEE PROFILE

Numerical Simulation of Scanning Electrochemical Microscopy Experiments with Frame-Shaped Integrated Atomic Force Microscopy–SECM Probes Using the Boundary Element Method

Oleg Sklyar,[†] Angelika Kueng,[‡] Christine Kranz,^{*,‡} Boris Mizaikoff,[‡] Alois Lugstein,[§] Emmerich Bertagnolli,[§] and Gunther Wittstock^{*,†}

School of Mathematics and Natural Sciences, Carl Von Ossietzky University of Oldenburg, D-26111 Oldenburg, Germany, School of Chemistry and Biochemistry, Georgia Institute of Technology, Atlanta, Georgia 30332-0400, and Institut für Festkörperelektronik & Mikrostrukturzentrum der TU–Wien, Floragasse 7, A-1040 Wien, Austria

Integrated submicroelectrodes for combined AFM–SECM measurements are characterized with numerical simulations using the boundary element method. SECM approach curves and SECM images are calculated and analyzed for a model substrate containing pronounced topographical and electrochemical features. The theoretically calculated image has been compared to the experimental data and shows excellent quantitative agreement. Hence, the applicability of integrated AFM–SECM electrodes for combined electrochemical and topographical imaging and a profound theoretical description including quantification of the obtained results are demonstrated.

Since the introduction of scanning tunneling microscopy (STM) by Rohrer and Binnig¹ scanning probe microscopic (SPM) techniques have developed into a range of powerful imaging and characterization tools for a wide variety of scientific disciplines. Atomic force microscopy (AFM)² is among the most versatile techniques, as its application is not limited to a certain nature of investigated samples. Furthermore, AFM measurements can be performed at ambient conditions, in a vacuum, and in liquid.³

Although superior resolution to the atomic level can be achieved, SPM techniques are frequently deficient on chemical information. To date, functionalizing scanning probes and the combination of SPM with appropriate surface chemistries are the most commonly applied techniques adding chemical specificity to SPM. Standard immobilization strategies are readily adapted for tethering biological recognition elements to scanning probe tips.⁴ Single-molecule force spectroscopy^{5–8} and force recognition

imaging^{9,10} have developed into powerful tools for high-resolution studies of molecular recognition events and for probing dynamic properties of biomolecules at physiological conditions. However, high temporal resolution remains a challenge of this approach.

In contrast to direct probe modification, the combination of complementary SPM techniques provides spatially correlated information on both morphology and surface chemistry, as demonstrated by combining scanning electrochemical microscopy (SECM) with STM, AFM, or near-field scanning optical microscopy (NSOM).

The fundamental principles of SECM have been introduced almost two decades ago.^{11–13} Since then, SECM has matured to a versatile analytical technique providing spatially resolved electrochemical information on interfacial processes. SECM operates by combining electroanalytical techniques based on ultramicroelectrodes (UME) with the principle of scanning a probe in close vicinity across the sample surface. The resulting two-dimensional images of surface-induced Faradaic currents measured at the biased probe-UME are obtained in dependence of the probe position. These Faradaic currents are predominantly controlled by the mass transport of redox species from the sample surface and from the bulk solution toward the UME. If microelectrodes are applied, steady-state signals are obtained.

The major drawback of SECM compared to AFM and other SPM techniques is the lack of sufficient lateral resolution in the constant-height imaging mode. As the UME current depends on

* Corresponding authors. E-mail: Gunther.Wittstock@Uni-Oldenburg.de. Christine.Kranz@chemistry.gatech.edu.

[†] Carl Von Ossietzky University of Oldenburg.

[‡] Georgia Institute of Technology.

[§] Festkörperelektronik & Mikrostrukturzentrum der TU–Wien.

(1) Binnig, G.; Rohrer, H.; Gerber, C.; Weibel, E. *Phys. Rev. Lett.* **1982**, *49*, 57–61.

(2) Binnig, G.; Quate, C. F.; Gerber, C. *Phys. Rev. Lett.* **1986**, *56*, 930–933.

(3) Drake, B.; Prater, C. B.; Weisenhorn, A. L.; Gould, S. A. C.; Albrecht, T. R.; Quate, C. F.; Cannell, D. S.; Hansma, H. G.; Hansma, P. K. *Science* **1989**, *243*, 1586–1589.

(4) Raiteri, R.; Grattarola, M.; Butt, H.-J.; Skladal, P. *Sens. Actuators, B* **2001**, *B79*, 115–126.

(5) Janshoff, A.; Neitzert, M.; Oberdörfer, Y.; Fuchs, H. *Angew. Chem., Int. Ed.* **2000**, *39*, 3212–3237.

(6) Willemsen, O. H.; Snel, M. M. E.; Cambi, A.; Greve, J.; De Grooth, B. G.; Figdor, C. G. *Biophys. J.* **2000**, *79*, 3267–3281.

(7) Carrion-Vazquez, M.; Oberhauser, A. F.; Fisher, T. E.; Marszalek, P. E.; Li, H.; Fernandez, J. M. *Prog. Biophys., Mol. Biol.* **2000**, *74*, 63–91.

(8) Zlatanova, J.; Lindsay, S. M.; Leuba, S. H. *Prog. Biophys., Mol. Biol.* **2000**, *74*, 37–61.

(9) Hinterdorfer, P. *Methods Cell Biol.* **2002**, *68*, 115–139.

(10) Raab, A.; Han, W.; Badt, D.; Smith-Gill, S. J.; Lindsay, S. M.; Schindler, H.; Hinterdorfer, P. *Nat. Biotechnol.* **1999**, *17*, 902–905.

(11) Liu, H. Y.; Fan, F.-R. F.; Lin, C. W.; Bard, A. J. *J. Am. Chem. Soc.* **1986**, *108*, 3838–3839.

(12) Engstrom, R. C.; Weber, M.; Wunder, D. J.; Burgess, R.; Winquist, S. *Anal. Chem.* **1986**, *58*, 844–848.

(13) Engstrom, R. C.; Meany, T.; Tople, R.; Wightman, R. M. *Anal. Chem.* **1987**, *59*, 2005–2010.

sample reactivity,¹⁴ the distance regulation of the probe via the current signal (constant current mode) is not feasible. The lateral resolution is limited by the dimensions of the electroactive surface of the UME. Although several approaches for the fabrication of nanoelectrodes have been published in the literature,^{15–20} their application to SECM is still limited due to the required decrease of the working distance d proportionally to the probe size. As a result, the roughness and the tilt of the sample surface are no longer negligible if small probes with corresponding probe–sample distances are applied. The first approach utilizing probe positioning in SECM was published in 1995.²¹ It was based on the integration of the shear force principle initially developed for NSOM into SECM. Recently, several applications of SECM using the shear force-based constant-distance mode have been reported.^{22–25} UME fabrication based on etching or laser-pulling procedures followed by conventional electrochemical insulation steps enabled the combination of SECM with ECSTM^{26,27} and AFM.^{28,29}

An alternative approach combining AFM and SECM is based on the integration of a defined electroactive area into AFM tips using microfabrication techniques.^{30,31} Submicrometer- and nanometer-sized electrodes with different defined geometries (e.g., frame, ring, disk) can be integrated at an exactly defined distance above the apex of the AFM tip, maintaining the integrity of the original AFM tip.^{32,33} Since the electroactive area is recessed from the very end of the combined probe, high-resolution AFM imaging and electrochemical SECM imaging can be simultaneously performed. The required constant distance between the integrated electrode and the sample surface is inherently maintained by the AFM tip. Recently, the application of such combined AFM–SECM probes for dynamic mode AFM operation has been demon-

strated,³⁴ including imaging of enzymatic activity of species immobilized in soft polymer samples.³⁵ Although the size of combined probes based on this approach is to date larger than the achievable dimensions of AFM–SECM probes based on bent Pt wires or of etched ECSTM–SECM probes, reproducible fabrication utilizing standard microfabrication processes and the precise knowledge of the UME–sample distance d and the electrode geometry renders this technology the first choice for quantitative treatment of heterogeneous reaction rates.

The possibility to relate experimental SECM data to a quantitative theoretical description is a major asset of SECM compared to other SPM techniques. In proximity to the sample surface, hemispherical diffusion profiles of redox species are influenced by the sample morphology, the interfacial reactions at the sample surface, the distance d between the UME and the sample surface, and the geometry of the UME and its insulating shielding. The corresponding set of these parameters can be used as input data for mathematical models and numerical tools for quantitative treatment. The mass transport characteristics of SECM have theoretically been described for a variety of experimental conditions and some basic UME geometries.^{36–42} Because the mathematical solution in SECM is very complex, numerical simulations have been introduced to the theory of SECM. Usually, modifications of the finite difference method (FDM) and the finite element method (FEM) were applied.^{43–51} However, the complexity of their implementation limits the utility of these techniques for three-dimensional (3D) considerations. Therefore, all SECM simulations using these techniques were performed in an axisymmetric two-dimensional (2D) space. This has limited the theoretical treatment of SECM to planar samples with homogeneous distribution of the reactivity and axisymmetric probes (disk, ring, cone, hemisphere) moving perpendicularly to the sample surface, i.e., the simulation of SECM approach curves. By comparing experimental approach curves to curves obtained by simulation, quantitative information can be extracted on both the UME size and the heterogeneous reaction rate at the sample surface.

Combined AFM–SECM and STM–SECM probes usually do not feature axial symmetry due to limited control on exact

(14) Bard, A. J.; Fan, F. R. F.; Mirkin, M. V. In *Electroanalytical Chemistry*; Bard, A. J., Ed.; Marcel Dekker: New York, 1994; Vol. 18, p 268.
 (15) Nagahara, L. A.; Thundat, T.; Lindsay, S. M. *Rev. Sci. Instrum.* **1989**, *60*, 3128–3130.
 (16) Penner, R. M.; Heben, M. J.; Longin, T. L.; Lewis, N. S. *Science* **1990**, *250*, 1118–1121.
 (17) Shao, Y.; Mirkin, M. V.; Fish, G.; Kokotov, S.; Palanker, D.; Lewis, A. *Anal. Chem.* **1997**, *69*, 1627–1634.
 (18) Sun, P.; Zhang, Z.; Guo, J.; Shao, Y. *Anal. Chem.* **2001**, *73*, 5346–5351.
 (19) Katemann, B. B.; Schuhmann, W. *Electroanalysis* **2002**, *14*, 22–28.
 (20) Chen, S.; Kucernak, A. *Electrochem. Commun.* **2002**, *4*, 80–85.
 (21) Ludwig, M.; Kranz, C.; Schuhmann, W.; Gaub, H. E. *Rev. Sci. Instrum.* **1995**, *66*, 2857–2860.
 (22) Hengstenberg, A.; Kranz, C.; Schuhmann, W. *Chem. Eur. J.* **2000**, *6*, 1547–1554.
 (23) James, P. J.; Garfias – Mesias, L. F.; Moyer, P. J.; Smyrl, W. H. *J. Electrochem. Soc.* **1998**, *145*, L64–L66.
 (24) Büchler, M.; Kelley, S. C.; Smyrl, W. H. *Electrochem. Solid State Lett.* **2000**, *3*, 35–38.
 (25) Oyamatsu, D.; Hirano, Y.; Kanaya, N.; Mase, Y.; Nishizawa, M.; Matsue, T. *Bioelectrochemistry* **2003**, *60*, 115–121.
 (26) Williams, D. E.; Mohiuddin, T. F.; Zhu, Y. Y. *J. Electrochem. Soc.* **1998**, *145*, 2664–2672.
 (27) Treutler, T. H.; Wittstock, G. *Electrochim. Acta* **2003**, *48*, 2923–2932.
 (28) Macpherson, J. V.; Unwin, P. R. *Anal. Chem.* **2000**, *72*, 276–285.
 (29) Macpherson, J. V.; Unwin, P. R. *Anal. Chem.* **2001**, *73*, 550–557.
 (30) Kranz, C.; Friedbacher, G.; Mizaikoff, B.; Lugstein, A.; Smoliner, J.; Bertagnolli, E. *Anal. Chem.* **2001**, *73*, 2491–2500.
 (31) Kranz, C.; Mizaikoff, B.; Lugstein, A.; Bertagnolli, E. In *Electrochemical Methods for the Environmental Analysis at Trace Element Biogeochemistry*; Taillefer, M.; Rozan, T. F., Eds.; American Chemical Society Symposium 320; American Chemical Society: Washington, DC, 2002.
 (32) Lugstein, A.; Bertagnolli, E.; Kranz, C.; Mizaikoff, B. *Surf. Interface Anal.* **2002**, *33*, 146–150.
 (33) Lugstein, A.; Bertagnolli, E.; Kranz, C.; Kueng, A.; Mizaikoff, B. *Appl. Phys. Lett.* **2002**, *81*, 349–351.

(34) Kueng, A.; Kranz, C.; Mizaikoff, B.; Lugstein, A.; Bertagnolli, E. *Appl. Phys. Lett.* **2003**, *82*, 1592–1594.
 (35) Kueng, A.; Kranz, C.; Mizaikoff, B.; Lugstein, A.; Bertagnolli, E. *Angew. Chem., Int. Ed.* **2003**, *42*, 3237–3240.
 (36) Bard, A. J.; Fan, F. R. F.; Mirkin, M. V. In *Electroanalytical Chemistry*; Bard, A. J., Ed.; Marcel Dekker: New York, 1994; Vol. 18, pp 243–373.
 (37) Mirkin, M. V.; Horrocks, B. R. *Anal. Chim. Acta* **2000**, *406*, 119–146.
 (38) Amphlett, J. L.; Denuault, G. *J. Phys. Chem. B* **1998**, *102*, 9946–9951.
 (39) Fulian, Q.; Fisher, A. C.; Denuault, G. *J. Phys. Chem. B* **1999**, *103*, 4387–4392.
 (40) Fulian, Q.; Fisher, A. C.; Denuault, G. *J. Phys. Chem. B* **1999**, *103*, 4393–4398.
 (41) Barker, A. L.; Macpherson, J. V.; Slevin, C. J.; Unwin, P. R. *J. Phys. Chem. B* **1998**, *102*, 1586–1598.
 (42) Liljeroth, P.; Johans, C.; Slevin, C. J.; Quinn, B. M.; Kontturi, K. *Anal. Chem.* **2002**, *74*, 1972–1978.
 (43) Kwak, J.; Bard, A. J. *Anal. Chem.* **1989**, *61*, 1221–1227.
 (44) Unwin, P. R.; Bard, A. J. *J. Phys. Chem.* **1991**, *95*, 7814–7824.
 (45) Zhou, F.; Unwin, P. R.; Bard, A. J. *J. Phys. Chem.* **1992**, *96*, 4917–4924.
 (46) Bard, A. J.; Mirkin, M. V.; Unwin, P. R.; Wipf, D. O. *J. Phys. Chem.* **1992**, *96*, 1861–1868.
 (47) Mirkin, M.; Fan, F. R. F.; Bard, A. J. *J. Electroanal. Chem.* **1992**, *328*, 47–62.
 (48) Selzer, Y.; Mandler, D. *Anal. Chem.* **2000**, *72*, 2383–2390.
 (49) Lee, Y.; Amemiya, S.; Bard, A. J. *Anal. Chem.* **2001**, *73*, 2261–2267.
 (50) Zoski, C. G.; Aguilar, J. C.; Bard, A. J. *Anal. Chem.* **2003**, *75*, 2959–2966.
 (51) Nann, T.; Heinze, J. *Electrochim. Acta* **2003**, *48*, 3975–3980.

electrode geometries at the nanometer scale. Moreover, the strength of SECM as an imaging technique is based on 2D imaging providing information on localized (electro)chemical activity at the sample surface. However, to theoretically describe such measurements, 3D simulations are required. Fulian et al.^{39,40,52} introduced the use of the boundary element method (BEM) for the numerical simulation of SECM problems. In a previous contribution,⁵³ we extended this approach to true 3D models and achieved improved accuracy by using the exterior formulation of the Laplace problem via open simulation domains. This approach enabled the quantitative simulation of 3D steady-state problems for asymmetric microelectrodes and nanoelectrodes.^{53–55}

In this contribution, the first comprehensive theoretical description of integrated AFM–SECM micro- and submicroframe electrodes (“integrated AFM–SECM probes”) and their application for combined AFM–SECM measurements is presented. A gold/silicon sample containing distinct conducting and insulating regions was selected as a model substrate. Experimentally obtained SECM images recorded in the SECM feedback/AFM contact mode at this sample surface were compared with the results of corresponding BEM simulations.

EXPERIMENTAL SECTION

Measurement Parameters and Instrumentation. The investigated sample was a silicon wafer, which was coated by sputtering with a gold layer (thickness, 100 nm) using a gold mesh (1500 mesh, SPI Supplies, West Chester, PA) as a mask. After removal of the mesh mask, conducting quadratic gold areas ($20 \times 20 \mu\text{m}$) remained at the insulating substrate surface.

All simultaneously recorded electrochemical and topographical data were obtained using a Nanoscope III atomic force microscope (Digital Instruments, Santa Barbara, CA) with a scan head providing a maximum imaging range of $125 \times 125 \mu\text{m}$. Investigations in solution were performed in a conventional liquid cell. For combined electrochemical and topographical measurements, the AFM was shielded with a home-built Faraday cage protecting the contact mode base and fluid cell of the Nanoscope III instrument. Simultaneous topographical and electrochemical imaging was performed in AFM contact mode and SECM feedback mode using 20 (for cyclic voltammetry) and 50 mmol L⁻¹ (for combined AFM–SECM imaging) [Fe(CN)₆]⁴⁻ in 0.5 mol L⁻¹ KCl as a redox mediator. K₄[Fe(CN)₆]⁴⁻ and KCl were purchased from Fluka (Milwaukee, WI). All other chemicals were of analytical grade; the solvents were of HPLC quality.

A three-electrode setup was used with a silver wire (Good-fellow) as silver quasi-reference electrode (AgQRE), a platinum wire as auxiliary electrode, and the AFM tip integrated UME as the working electrode. All potentials are referred to the AgQRE used in the experiments. The UME was held at a potential of +0.6 V versus AgQRE. The scan area was $40 \times 40 \mu\text{m}^2$ at a scan rate of 1 Hz. Potential control and current measurements were

performed with a CH Instruments bipotentiostat (832A, Austin, TX). The signal output of the bipotentiostat was connected to the data acquisition board of the AFM using a signal access module (Digital Instruments, Santa Barbara, CA) allowing direct correlation of the electrochemical data with the topographical information. All images were recorded in contact mode operation with 256 lines/scan.

Integrated AFM–SECM Probes. For the fabrication of combined AFM–SECM probes, commercially available silicon nitride AFM cantilevers (Veeco Instruments, Santa Barbara, CA; length 200 μm , nominal spring constant 0.06 N m⁻¹, pyramidal tip base $4 \times 4 \mu\text{m}^2$, and tip height 2.86 μm) were coated with a gold layer (100 nm) and then insulated with a xylylene polymer (Parylene C) by vapor deposition polymerization.⁵⁶ 3D focused ion beam (FIB) milling was used to expose the electroactive area and to precisely correlate the length of the AFM tip with the electrode dimensions. A detailed description of integrated AFM–SECM probe fabrication is given elsewhere.^{30,33} The integrated AFM–SECM probe applied in the presented study had an outer edge length f of 670 nm, an electrode layer thickness w_f of 100 nm, and a reshaped tip height h_t of 400 nm (Figure 1a and b).

Simulation Tools. Simulations with the BEM were performed with an in-house-developed software⁵⁵ written in C++ on a Linux-PC with a 2-GHz processor and 512 MB of RAM. The average computation time was ~ 2 –3 min for a single geometric configuration of ~ 2000 mesh elements and required 320 MB of memory. A whole image consisting of 50×50 data points could be calculated in 35 h. The following algorithms were used in the overall BEM setup: the Gauss–Legendre 13-point quadrature rules for numerical integration and analytical two-dimensional surface integration, the LU decomposition for solution of dense linear systems, and the Delaunay triangulation for composing the mesh. A separate geometry editor was created and used for mesh development and assignment of boundary conditions to mesh elements.

RESULTS AND DISCUSSION

BEM Simulations. Integrated AFM–SECM probes positioned above a sample with areas of different reactivity represent a complex simulation task due to the absence of axial symmetry. Additional complications arise from the morphology of the sample, which is traced with the electrode at a constant distance via the free-standing reshaped AFM tip. This implies that different sections of the frame electrode will have different distances to the sample surface when moving across a topographic feature. As previously discussed, the BEM allows treatment of true 3D situations that cannot be cast into a 2D problem. Since the fundamentals of the BEM have thoroughly been reviewed by Brebbia and Kirkup,^{57,58} and SECM-specific issues have recently been addressed,^{53,55} this contribution outlines only a minimum of algorithms facilitating understanding of the simulation setup for the specific case of integrated SECM-AFM probes, which represents a methodical advance compared to ref 53.

(52) Fulian, Q.; Fisher, A. C.; Denuault, G. *J. Phys. Chem. B* **1998**, *102*, 9647–9652.

(53) Sklyar, O.; Wittstock, G. *J. Phys. Chem. B* **2002**, *106*, 7499–7508.

(54) Sklyar, O.; Ufheil, J.; Heinze, J.; Wittstock, G. *Electrochim. Acta* **2003**, *48*, 117–128.

(55) Sklyar, O. Dissertation, Modelling Scanning Electrochemical Microscopy (SECM) Experiments on Microstructured Functionalised Surfaces. University of Oldenburg, 2004.

(56) Heintz, E. L. H.; Kranz, C.; Mizaikoff, B.; Noh, H.-S.; Hesketh, P.; Lugstein, A.; Bertagnolli, E. *Proc. IEEE Nanotechnol. Conf.* 2001.

(57) Brebbia, C. A.; Dominguez, J. *Boundary Elements: An Introductory Course*; Computational Mechanics Publications, Southampton, England, and Elsevier: New York, 1994.

(58) Kirkup, S. *The BEM for Laplace Problems*; ISS, www.boundary-element-method.com.

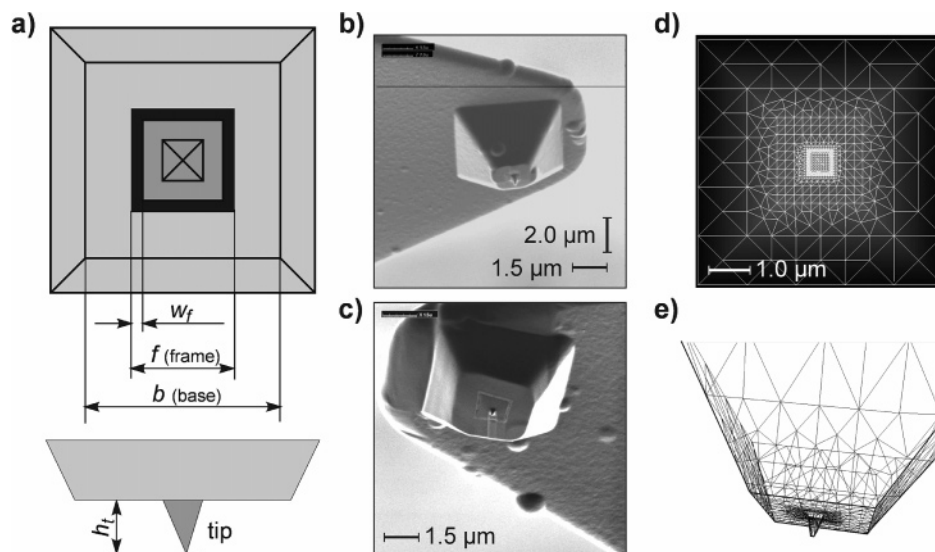


Figure 1. (a) Schematic bottom and side views of the combined AFM-SECM probes with nomenclature. Shades of gray indicate different materials: dark gray, silicon nitride of the original AFM cantilever; black, gold electrode; light gray, parylene; (b) and (c) SEM images of combined AFM-SECM probes: (b) $f = 670$ nm, $w_f = 100$ nm, $h_t = 400$ nm (used for imaging in Figure 4), (c) $f = 1520$ nm, $w_f = 100$ nm, $h_t = 580$ nm; (d) boundary mesh for the combined AFM-SECM probe in (b) and its 3D representation in (e).

The electroactive area of the integrated AFM-SECM probe is used to oxidize $[\text{Fe}(\text{CN})_6]^{4-}$ (denoted as R) at +0.6 V versus AgQRE under close to diffusion-controlled conditions. For simulations, the reaction can be characterized by a rate constant k_f



The microstructured gold features of the test sample assume a potential dictated by the Nernst equation. Because the bulk solution contains only R, the reduction of $[\text{Fe}(\text{CN})_6]^{3-}$ (denoted as O) with the rate constant k_b proceeds at those sample regions located underneath the frame electrode moving across the sample features in constant distance.



For simplicity, equality is assumed for the diffusion coefficients of O and R ($D_O = D_R$). The total concentration c^* of R and O is conserved and is equal to the bulk concentration of R:

$$D_O = D_R = D \quad (3)$$

$$c_R(\mathbf{r}) + c_O(\mathbf{r}) = c^* \quad (4)$$

where $c_R(\mathbf{r})$ and $c_O(\mathbf{r})$ are the concentrations of R and O at point \mathbf{r} . The value of D was measured as $D = 7.1 \times 10^{-6} \text{ cm}^2 \text{ s}^{-1}$. Under the assumption of established steady-state diffusion, the mass transport equation system is reduced to a system of Laplace equations for $c_R(\mathbf{r})$ and $c_O(\mathbf{r})$, which can be reduced to a single equation for $c(\mathbf{r}) = c_O(\mathbf{r})$ utilizing eq 4

$$\partial c(\mathbf{r}, t) / \partial t = 0 = \nabla^2 c(\mathbf{r}), \mathbf{r} \in V \quad (5)$$

where ∇^2 is the Laplace operator and V is the simulation domain.

The BEM proceeds by transforming eq 5 into its integral representation at the domain boundary Γ according to Green's second identity and its further discretization at triangular boundary elements⁵³

$$\frac{1}{2}c(\mathbf{r}_i) = \sum_{j=1}^N \frac{\partial c(\mathbf{r}_j)}{\partial \mathbf{n}_j} \int_{\Gamma_j} G(\mathbf{r}, \mathbf{r}_j) d\Gamma - \sum_{j=1}^N c(\mathbf{r}_j) \int_{\Gamma_j} \frac{\partial G(\mathbf{r}, \mathbf{r}_j)}{\partial \mathbf{n}_j} d\Gamma \quad (6)$$

where for one specific element i , the sum over all boundary elements indexed by j is taken with values of concentration $c(\mathbf{r}_j)$ and flux $\partial c(\mathbf{r}_j) / \partial \mathbf{n}_j$. $G(\mathbf{r}, \mathbf{r}_j) = 1/4\pi|\mathbf{r}_i - \mathbf{r}_j|$ is the standard Green function for the Laplace equation calculated from the absolute distance $|\mathbf{r}_i - \mathbf{r}_j|$ between the elements i and j .

Previous experience has shown that the simulation results are stabilized if situations are avoided where elements with boundary conditions of Neumann-type (constant flux) and Dirichlet-type (constant concentration) coexist within one enclosed object. Therefore, in this contribution, Robin-Couchy boundary conditions specifying a linear combination between the flux and the concentration were used instead of Dirichlet-type boundary conditions. For the integrated frame electrode these boundary conditions are given by

$$D(\partial c / \partial \mathbf{n}) = k_f c \quad (7)$$

and for the conductive gold regions at the sample surface by

$$D(\partial c / \partial \mathbf{n}) = -k_b c \quad (8)$$

For the reaction at the UME, k_f is set to a high value (10^3). This is equivalent to the Dirichlet-type boundary condition $c = c^*$

describing diffusion-controlled reactions; however, it avoids the associated numerical singularity problem. Rate constants larger than 10 result in calculated probe currents with negligible deviations, because the reaction is essentially diffusion controlled. At the insulating sections of the combined AFM–SECM probe and at the insulating parts of the sample no flux is allowed across the boundary. This leads to Newman-type boundary conditions

$$\frac{\partial c}{\partial \mathbf{n}} = \frac{\partial c_O}{\partial \mathbf{n}} = \frac{\partial c_R}{\partial \mathbf{n}} = 0 \quad (9)$$

The solution stability was further enhanced according to the recommendations of Kirkup⁵⁹ and according to our own test results.⁵⁵ For every element i , the system equation was composed from a linear combination of eq 6 and from its derivative with respect to the surface normal \mathbf{n}_i . Discretization similar to the algorithm used to obtain eq 6 yields

$$\begin{aligned} \frac{1}{2} \left(c(\mathbf{r}_i) + \frac{\partial c(\mathbf{r}_i)}{\partial \mathbf{n}_i} \right) &= \sum_{j=1}^N \frac{\partial c(\mathbf{r}_j)}{\partial \mathbf{n}_j} \int_{\Gamma_j} G(\mathbf{r}_i, \mathbf{r}_j) d\Gamma - \\ &\sum_{j=1}^N c(\mathbf{r}_j) \int_{\Gamma_j} \frac{\partial G(\mathbf{r}_i, \mathbf{r}_j)}{\partial \mathbf{n}_j} d\Gamma + \sum_{j=1}^N \frac{\partial c(\mathbf{r}_j)}{\partial \mathbf{n}_j} \int_{\Gamma_j} \frac{\partial G(\mathbf{r}_i, \mathbf{r}_j)}{\partial \mathbf{n}_i} d\Gamma - \\ &\sum_{j=1}^N c(\mathbf{r}_j) \int_{\Gamma_j} \frac{\partial^2 G(\mathbf{r}_i, \mathbf{r}_j)}{\partial \mathbf{n}_i \partial \mathbf{n}_j} d\Gamma \quad (10) \end{aligned}$$

The combined eq 10 stabilizes the solution with respect to adjacent boundary conditions of different types, i.e., of Neumann-type and Dirichlet-type. By running point i through all N boundary elements, a system of linear equation for $2N$ unknown $c(\mathbf{r}_j)$ and $\partial c(\mathbf{r}_j)/\partial \mathbf{n}_j$ is composed from eq 10. To solve eq 10, half of the unknowns are defined by the problem-specific boundary conditions. For the Robin–Couchy-type boundary conditions (eqs 7 and 8) used in this work, values of $\partial c(\mathbf{r}_j)/\partial \mathbf{n}_j$ in eq 10 were substituted with corresponding linear function of $c(\mathbf{r}_j)$, thus reducing the number of unknowns to N for N equations.

Combining all unknown values of $c(\mathbf{r}_j)$ and $\partial c(\mathbf{r}_j)/\partial \mathbf{n}_j$ in a single vector \mathbf{x} , all integrals of Green's function and its derivative in a single matrix \mathbf{A} , and all values obtained from the boundary conditions in a vector \mathbf{b} , the final system of linear equations can be written in matrix form as

$$\mathbf{A} \times \mathbf{x} = \mathbf{b} \quad (11)$$

and solved using conventional numerical procedures.

The flux at the integrated AFM–SECM frame UME can be directly obtained by summation of the fluxes at all elements N_{el} describing the frame electrode surface with

$$i_T \approx nFD \sum_i \int_{\Gamma_{\text{el},i}} \frac{\partial c_i}{\partial \mathbf{n}_i} d\Gamma_{\text{el},i} = nFD \sum_i \left(\frac{\partial c_i}{\partial \mathbf{n}_i} \Gamma_{\text{el},i} \right) \quad (12)$$

where $n = 1$ is the number of electrons transferred in a redox event and F is the Faraday constant.

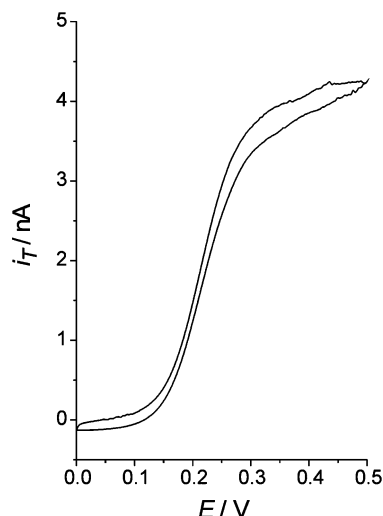


Figure 2. Cyclic voltammogram of the integrated AFM–SECM electrode (in Figure 1c). Mediator: 20 mM $[\text{Fe}(\text{CN})_6]^{4-}$ in 0.5 M KCl, reference electrode AgQRE, scan rate 100 mV s^{−1}.

Geometry of the SECM–AFM Tips and Their Representation in BEM Simulations. Figure 1b shows an ion-induced secondary electron image (“FIB image”) of the combined AFM–SECM probe used for the measurements in this paper. Details of the geometry are schematically shown in Figure 1a. Complex geometries can be approximated by a set of conformal triangles such as shown in Figure 1d and e for the combined AFM–SECM probe. The geometry was constructed from a drawing similar to Figure 1a with a height-proportional coloration of the surface. The mesh was formed at this surface by a combination of an automated routine providing some standard mesh shapes and manual refinement. A denser mesh is used to describe the active electrode surface and surrounding areas where high variations of local flux and local concentration can be expected. Boundary conditions are defined and assigned to each mesh element. Figure 1d shows a top view on the mesh. The colors of the mesh elements indicate the type of boundary condition assigned to them. The same in-house geometry editor was used to generate the mesh for the sample. The mesh data with associated boundary conditions constitute unified input data for the numerical simulation itself, which operates completely independent from the particular system geometry.

The meshes for the probe and the sample are positioned with respect to each other and the current i_T at a particular tip position is obtained from eq 12 after solving eq 10. Using open simulation domains, the two objects are then repositioned without changing the meshes of the probe and the sample itself.⁵³ Because of the nature of the BEM, the procedure can be repeated without any mesh generation for the solution volume. This possibility constitutes a dramatic advantage over FEM and FDM simulations, where the solution mesh and its refinements are required whenever the relative position of the probe changes above an uneven surface or above a surface with nonhomogeneous distribution of reaction rates.

Characterization of Integrated AFM–SECM Frame Electrodes. The integrated electrode in Figure 1c was experimentally

(59) Kirkup, S. *Fortran codes for Laplace problems in 2D and 3D*; www.boundary-element-method.com.

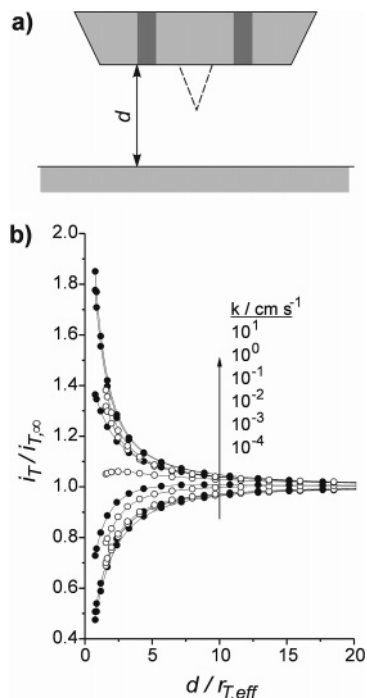


Figure 3. (a) Schematic side view of the combined AFM–SECM probe for simulations of approach curves; (b) calculated normalized approach curves with different values of reaction rate constants at the sample k_b in 20 mM $[\text{Fe}(\text{CN})_6]^{4-}$ at $D = 7.1 \times 10^{-6} \text{ cm}^2 \text{ s}^{-1}$: open dots, electrode in Figure 1b ($h/r_{T,\text{eff}} \approx 1.6$); solid dots, electrode in Figure 1c ($h/r_{T,\text{eff}} \approx 0.77$). Corresponding solid lines, calculated approach curves for the same geometries without a tip. RG values of electrodes are approximately 4 (for electrode in Figure 1b) and 2.5 (for electrode in Figure 1c) as estimated from FIB images in Figure 1b and c.

characterized by cyclic voltammetry (CV). The CV in Figure 2 shows a typical behavior for microelectrode reaching the steady-state current at potentials higher than +0.45 V. The working potential was selected from the CV at the level of +0.6 V. The value of the steady-state diffusion-controlled current, $i_{T,\infty}$ can be estimated from the CV at $4.5 \pm 0.3 \text{ nA}$ with small charging currents evident in the CV. The theoretical value of $i_{T,\infty}$ was calculated for the same electrode and at the same conditions at $7.45 \pm 0.05 \text{ nA}$. The calculation was performed by assuming only the combined AFM–SECM probe in the infinitely large solution (simulation domain). Discrepancy may result from adsorbed material onto the integrated frame electrode, which limits the reaction rate. In future, an improved cleaning step during FIB milling along with electrochemical cleaning of the integrated electrode surface should reduce this discrepancy.

During imaging, the integrated AFM–SECM frame electrode maintains a constant working distance d to the sample surface defined by the height of the reshaped AFM tip (h). However, it was previously shown that this does not eliminate the topographical effect on i_T .⁵³ Furthermore, in contrast to ring electrodes or other conventional SECM probes, currents measured at the combined AFM–SECM probe might be affected by the presence of the free-standing reshaped AFM tip, which is an obstacle to mass transport toward the integrated electrode. To analyze the effect of the tip on the SECM signal, approach curves were calculated for a given combined AFM–SECM probe and the same probe without a reshaped tip (Figure 3a).

The calculated normalized approach curves for the integrated frame electrodes in Figure 1b and c are given in Figure 3b represented by open and solid dots, respectively. The approach curves were calculated for different values of the reaction rate constant k_b at a planar sample with a homogeneous distribution of the reaction rate constant. For the normalization, values of $i_{T,\infty}$ were separately calculated as 1.99 ± 0.05 and $7.45 \pm 0.05 \text{ nA}$ (in 20 mM $[\text{Fe}(\text{CN})_6]^{4-}$) corresponding to the probes in Figure 1b and c. First, a typical change of the approach curve characteristics for microelectrodes of different RG values can be observed. Here, the RG values can be estimated from FIB images in Figure 1b and c as the ratio of the base b to f (see Figure 1a) at a value of 4 and 2.5 for the electrodes in Figure 1b and c, respectively. In the same figure, solid lines represent the results for the same electrode geometries but without having a tip. As clearly indicated in Figure 3b, the differences between the electrodes with and without the tip clearly rest within the numerical errors, which generally do not exceed 1% depending on the complexity of the mesh and its level of details. Additionally, SECM approach curves for integrated probes with and without tips were calculated for a planar sample divided into two sections: one section was kept at $k_b = 10^{-4} \text{ cm s}^{-1}$ (inert part) and the other section was kept at $k_b = 10 \text{ cm s}^{-1}$, which describes a diffusion-controlled reaction at the conductive part (see also discussion following eq 8). The tip was positioned at the border of the two regions. At these conditions, differences between currents for probes with and without tips should be maximized. The normalized current for both situations was close to 1, decreasing from 1.06 to 1.01 as the normalized distance increases. The differences between cases with and without the tip were at maximum 2%. Hence, it is confirmed that even in the most critical situation the presence of the protruding tip does not significantly influence the results.

SECM approach curves also provide information on the sensitivity of such combined probes to changes in surface reactivity. For the frame electrode used in this study for simultaneously recording electrochemical and topographical information, the working distance constituted 400 nm, which corresponds to $h/r_{T,\text{eff}} = 1.6$. The effective electrode radius $r_{T,\text{eff}}$ is calculated as a radius of a circle with the same area as the active area of the frame electrode. At the same time, standard working distances for conventional SECM operation in the feedback mode are usually selected in the range of $0.5r_T - 1.0r_T$ to ensure sufficient sensitivity. Obviously, the sensitivity of the electrode shown in Figure 1c at $d = r_{T,\text{eff}}$ is higher than that of the electrode shown in Figure 1b. This difference results from the smaller relative distance between the electrode and the sample ($h/r_{T,\text{eff}} = 0.77$ as compared to $h/r_{T,\text{eff}} = 1.6$). Whereas probes with a smaller $h/r_{T,\text{eff}}$ result in higher sensitivity, the pyramidal body of the probe may limit the applicability of such electrodes at highly corrugated samples.

It is experimentally difficult to record SECM approach curves of integrated AFM–SECM electrodes with a conventional AFM setup. While the scan area of the AFM covers a distance of $\sim 125 \mu\text{m}$ in a lateral direction, the z -piezo of AFM does not allow precise scans in the z -direction over $\sim 10\text{--}20 \mu\text{m}$, which is required for approach curves recorded at electrodes of the given dimensions. Hence, a comparison to experimental approach curves is omitted in this study.

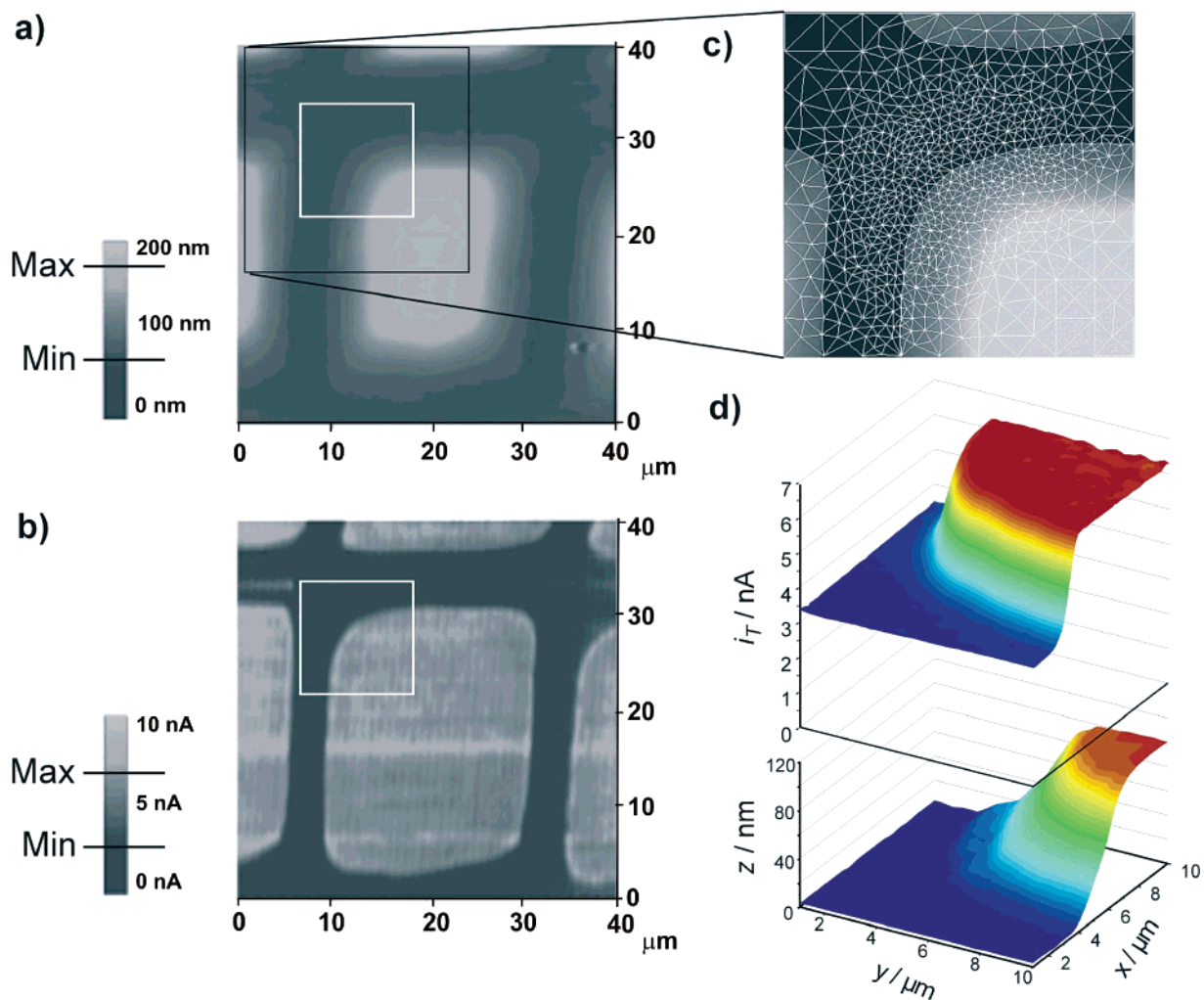


Figure 4. Experimental AFM contact mode image (a, topography) and simultaneously obtained SECM feedback image (b, current) measured with the integrated SECM-AFM electrode (in Figure 1b). White rectangles indicate scanning area for simulations, black rectangle in (a) indicates total sample area considered for simulations; (c) simulation mesh for the selected area; (d) simulated SECM feedback current in the area marked white in (a) and (b). Experimental and simulation parameters: 50 mM $[\text{Fe}(\text{CN})_6]^{4-}$ in 0.5 M KCl, $E_T = +0.6$ V vs AgQRE, scan rate = 1 Hz; $D = 7.1 \times 10^{-6} \text{ cm}^2 \text{ s}^{-1}$, calculated $i_{T,\infty} = 4.67$ nA, $r_{T,\text{eff}} = 255$ nm.

To provide a qualitative comparison of the obtained results with the investigations of ring electrodes by Lee et al.,⁴⁹ the ratio of the inner frame size to the outer frame size (a/b in the notation of Lee et al.) can be estimated at 0.7 and 0.9 for the electrode in Figure 1b and c, respectively. As indicated before, the RG values were correspondingly estimated at 4 and 2.5. Using these parameters, our results are in a good correlation with the data of Lee et al.⁴⁹ for RG values of ring electrodes at 3 and a/b between 0.8 and 0.9. The observed deviations are associated with the square shape of the frame electrode and rest within $\sim 5\%$ at most.

Combined AFM–SECM Imaging. The integrated probe shown in Figure 1b was applied for simultaneously recording AFM and SECM images of a test sample comprising a regular structure of gold islands ($20 \times 20 \mu\text{m}$) at the surface of an insulating substrate. The thickness of the gold islands increases from the edge toward the center as shown in the contact mode AFM image (Figure 4a). The size of the islands is more than 10 times larger than the dimensions of the integrated frame electrode, and one can therefore assume an almost diffusion-controlled reaction rate at the gold areas of the sample during SECM feedback experiments. The results of SECM imaging are shown together with

the corresponding topography provided by the reshaped AFM tip in Figure 4b. The sharp onset of electrochemical reactivity is clearly evident. The current above the gold region has a uniform magnitude apart from some noise. This result proves that the reshaped AFM tip effectively ensures a constant working distance even at protruding sample areas. The height of the gold island in the center is ~ 100 nm, which is 1/4 of the working distance (~ 400 nm). If the same experiment would be conducted without distance control (i.e., in constant height mode), this dramatic change of the working distance would be clearly evident in the recorded data set.

To simulate this experiment with the BEM method, the integrated probe was described by the mesh shown in Figure 1d. For the sample mesh, the topography image from the AFM scan was used as input for the geometry editor. The image was calculated for a small region of the sample featuring a topography and reactivity change (white squares in Figure 4a and b). Information obtained from this region essentially describes similar situations at other locations of the sample surface. As the topography and reactivity of adjacent sample sections may also affect the SECM signals above the selected region, a larger sample

segment was considered as input geometry for the simulation (dark square in Figures 4a). Therefore, the mesh describing the sample (in Figure 4c) extends to $\sim 20\text{ }\mu\text{m}$, which is 5 times larger than the base of the combined probe pyramid and ~ 80 times larger than the effective electrode radius. Furthermore, the distance between the electrode center and the edge of the considered sample region was at least $20r_{\text{T,eff}}$. Thus, it is ensured that the effect of the flux contribution from the bulk beneath the sample is negligible.

The heterogeneous rate constant k_b for the gold regions was set to 10^3 if the gold thickness exceeds 20 nm. This describes a diffusion-controlled reaction, which is discussed following eq 8. A reaction rate of zero was assumed for the rest of the sample. The simulated image is shown in Figure 4d. The calculated results precisely reproduce the sharp change of the SECM feedback current above the protruding gold island and agree with the experimentally measured currents at the integrated electrode. The calculated $i_{\text{T},\infty}$ is $4.67 \pm 0.05\text{ nA}$ (in 50 mM $[\text{Fe}(\text{CN})_6]^{4-}$). As expected, the current difference between insulating and conducting regions is comparable to the difference in the approach curves given in Figure 3b for $k_b = 10$ and 10^{-4} cm s^{-1} . The slightly smaller values obtained during the experiments may result from adsorptions at the sample or at the probe. The agreement of the theoretical and experimental values confirms that the combined AFM–SECM probes can be effectively applied to SECM measurements in the constant distance mode and that the proposed numerical simulation technique is capable of accurately processing such complex geometrical arrangements.

In both experimental data and simulation results, the transition region of the SECM response is much sharper than the topographic transition. This is a peculiarity of the current experiment. The topographical change is imaged across the entire gold island reflecting the thickness variation of the gold island from 0 to 100 nm. At the same time, as soon as the thickness of the island reaches 20 nm, it becomes conductive and leads to a positive feedback in the SECM signal, which remains constant as long as the working distance of the electrode to the sample surface remains constant. This is ensured in the combined AFM–SECM approach by the reshaped AFM tip. Because the size of the integrated frame is much smaller than the size of the island (a region of $80r_{\text{T,eff}}$ is used in the simulation), one can expect a relatively sharp signal transition during a horizontal SECM scan. Hence, the topographical features would not be comprehensively obtained by recording just the SECM image.

CONCLUSIONS

SECM images have been recorded with combined AFM–SECM tips comprising tip-integrated frame submicroelectrodes

during contact mode AFM operation. Numerical simulations with the boundary element method have quantitatively reproduced the experimental results and theoretically confirm the functionality of these bifunctional AFM–SECM probes. In contrast to existing simulations, the accuracy of the BEM algorithm was further improved and it could be shown that the influence of the reshaped AFM tip centered in the middle of the frame electrode on the response of an AFM tip-integrated frame electrode is negligible. It is demonstrated that the application of geometrically well-defined integrated AFM–SECM probes brings micro- and nano-SECM experiments close to the quantitative rigor typically encountered for disk-shaped UME probes with diameters of 10 or 25 μm . In addition, the reshaped AFM tip provides a well-defined current-independent distance regulation for the electroactive area during SECM experiments with no significant effects on the measured Faradaic currents.

Complementary to the innovative development and application of microfabricated bifunctional AFM–SECM tips, numerical simulation based on the boundary element method and the associated editing and calculation software have reached a level of maturity that allows treatment of highly complex 3D diffusion problems with finite reaction kinetics at the probe electrode and the sample on a routine basis in steady-state situations. In future, this novel route for bifunctional probe fabrication along with 3D simulations has the potential to facilitate the transition of quantitative SECM imaging applications from the microdomain to the nanodomain addressing samples with increasing complexity of topographic features and inhomogeneous distribution of interfacial reactivities, such as encountered in, for example, biological systems.

ACKNOWLEDGMENT

The National Science Foundation (Grant 0216368 within the program ‘Biocomplexity in the Environment’), the National Institute of Health (Grant EB000508), the ‘Fonds zur Förderung der wissenschaftlichen Forschung’ Austria (Grant J2230), and the Deutsche Forschungsgemeinschaft (Grant Wi1617/7) are greatly acknowledged for support of this work.

Received for review August 25, 2004. Accepted October 25, 2004.

AC048732N